Acquisition of object and temperature series in medium resolution off-axis electron holography with live drift correction

Supplementary Information

Thibaud Denneulin[a], Benjamin Zingsem[a], Joseph Vas[a], Wen Shi[a], Luyan Yang[a], Michael Feuerbacher[a] and Rafal E. Dunin-Borkowski[a]

[a]*Ernst Ruska-Centre for Microscopy and Spectroscopy with Electrons, Forschungszentrum Jülich, 52425 Jülich, Germany.*

Supplementary Information 1: Basics of off-axis electron holography

In off-axis electron holography, a voltage is applied to an electron biprism, which is inserted below the sample, generally in the selected area aperture position in order to overlap two electron waves. An interference pattern (the hologram) is recorded on a detector. We consider a reference wave $\psi_1 = A_1 \exp(i\phi_1)$ traveling in a uniform region (vacuum for instance) and an object wave $\psi_2 = A_2(\vec{r}) \exp(i\phi_2(\vec{r}))$ passing through a sample, where $A_1, A_2(\vec{r})$ and $\phi_1, \phi_2(\vec{r})$ are their respective amplitudes and phases. The intensity distribution of an off-axis electron hologram can be expressed

$$I_{holo}(\vec{r}) = A_1^2 + A_2^2(\vec{r}) + I_{\text{inel}}(\vec{r}) + 2\mu A_1 A_2(\vec{r}) \cos(\Delta\phi(\vec{r}) + 2\pi \vec{q_{\text{c}}}.\vec{r}) \ , \tag{1}$$

where $I_{\text{inel}}(\vec{r})$ is the inelastic background, μ is the fringe contrast, $\Delta\phi(\vec{r}) = \phi_1 - \phi_2(\vec{r})$ is the phase change of the object wave with respect to the reference wave and $\vec{q_{\text{c}}}$ is the carrier frequency [1]. The Fourier transform of the hologram can be described as

$$\begin{array}{rcll} \text{FT}\{I_{holo}(\vec{r})\} & = & \text{FT}\{A_1^2 + A_2^2(\vec{r}) + I_{\text{inel}}(\vec{r})\} & \textit{centerband} \\ & & +\mu\text{FT}\{A_1 A_2(\vec{r}) \exp(i\Delta\phi(\vec{r}))\} \otimes \delta(\vec{q} + \vec{q_{\text{c}}}) & \textit{sideband } 1 \\ & & +\mu\text{FT}\{A_1 A_2(\vec{r}) \exp(i\Delta\phi(\vec{r}))\} \otimes \delta(\vec{q} - \vec{q_{\text{c}}}) & \textit{sideband } 2 \quad . \end{array} \tag{2}$$

Different images can then be reconstructed by using apertures and inverse Fourier transforms such as

$$\begin{array}{rcccl} I_{\text{rec}}(\vec{r}) & = & A_1^2 + A_2^2(\vec{r}) + I_{\text{inel}}(\vec{r}) & & , \\ C_{\text{rec}}(\vec{r}) & = & \mu A_1 A_2(\vec{r}) \exp(i\Delta\phi(\vec{r})) & & , \\ A_{\text{rec}}(\vec{r}) & = & \mu A_1 A_2(\vec{r}) & = & \sqrt{Re^2 + Im^2} \quad , \\ \phi_{\text{rec}}(\vec{r}) & = & \Delta\phi(\vec{r}) & = & \arctan(Im/Re) \quad , \end{array} \tag{3}$$

where $I_{\text{rec}}(\vec{r})$ is the intensity image reconstructed by applying an aperture to the center-band. $C_{\text{rec}}(\vec{r})$ is the reconstructed complex image obtained after applying an aperture to one of the side-bands, shifting it to center of Fourier space and performing an inverse Fourier transform. $A_{\text{rec}}(\vec{r})$ and $\phi_{\text{rec}}(\vec{r})$ are the corresponding amplitude and phase obtained from the complex image. Usually, the radius of the aperture applied to the side-band is $q_{\text{c}}/3$ to avoid including information from the center-band.

If the effects of dynamical diffraction in the specimen can be neglected and if there are no fringing field outside the specimen, the phase change $\Delta\phi$ is related to electromagnetic fields according to the expression (in one dimension) [2]

$$\Delta\phi(x) = C_E \int V_0(x, z) dz - \frac{e}{\hbar} \iint B_\perp(x, z) dx dz \ , \tag{4}$$

where z is the direction of the incident electron beam, x is a direction perpendicular to z, C_E is an interaction constant that depends on the electron energy, V_0 is the mean inner potential (MIP) of the specimen, $B_\perp$ is the component of the magnetic induction field that is perpendicular to both x and z, e is the electron charge and $\hbar$ is the reduced Planck constant. If V_0 and $B_\perp$ are constant in the specimen along z, then the previous expression can be simplified to

$$\Delta\phi(x) = C_E V_0(x) t(x) - \frac{e}{\hbar} \int B_\perp(x) t(x) dx \ , \tag{5}$$

35 where t is the specimen thickness. In the case of a non-magnetic sample with uniform thickness, the phase
36 change is proportional to the MIP according to the expression

$$\Delta\phi(x) = C_E V_0(x) t \ . \tag{6}$$

37 In the case of a magnetic sample with uniform thickness and composition, the derivative of the phase is
38 proportional to the magnetic induction according to the expression

$$\frac{d(\Delta\phi(x))}{dx} = -\frac{e}{\hbar} B_{\perp}(x) \ . \tag{7}$$

Supplementary Information 2: Short description of the stage

Little information could be found about the design of the piezo-enhanced CompuStage. Nonetheless, Fig. S1(a) shows a picture of the stage taken after removal of the cover with the permission of Thermo Fischer Scientific (TFS). Users familiar with TFS microscopes can recognize the beta tilt plug, the red LED on the bottom left that indicates if the holder can be retracted/inserted and the holder entry at the center. The mechanical axes x, y and z are located at the top, left and bottom respectively. After discussion with TFS engineers, we understood that the stage is physically identical to other Titan stages but the piezo control option is obtained using additional cabling during the installation. Three cables controlling the x, y and z piezo components are attached on the right side of the stage. They are visible in Fig. S1(b) when the stage is tilted at a large α angle and they are connected to the mechanical shafts of the three axes. In addition, the piezo stage has its own electronic controller shown in Fig. S1(c) that is installed in a rack next to the microscope PC.

It should be mentioned that the use of a piezo stage in off-axis electron holography has been introduced in previous articles [3, 4], where it was used to scan the sample with respect to the fringes and hence improve the spatial resolution of the reconstructed phase images. However, the piezo components were integrated in a single tilt sample holder [5]. Here, the stage is part of the microscope, which allows different sample holders to be used and hence different experiments to be conducted.

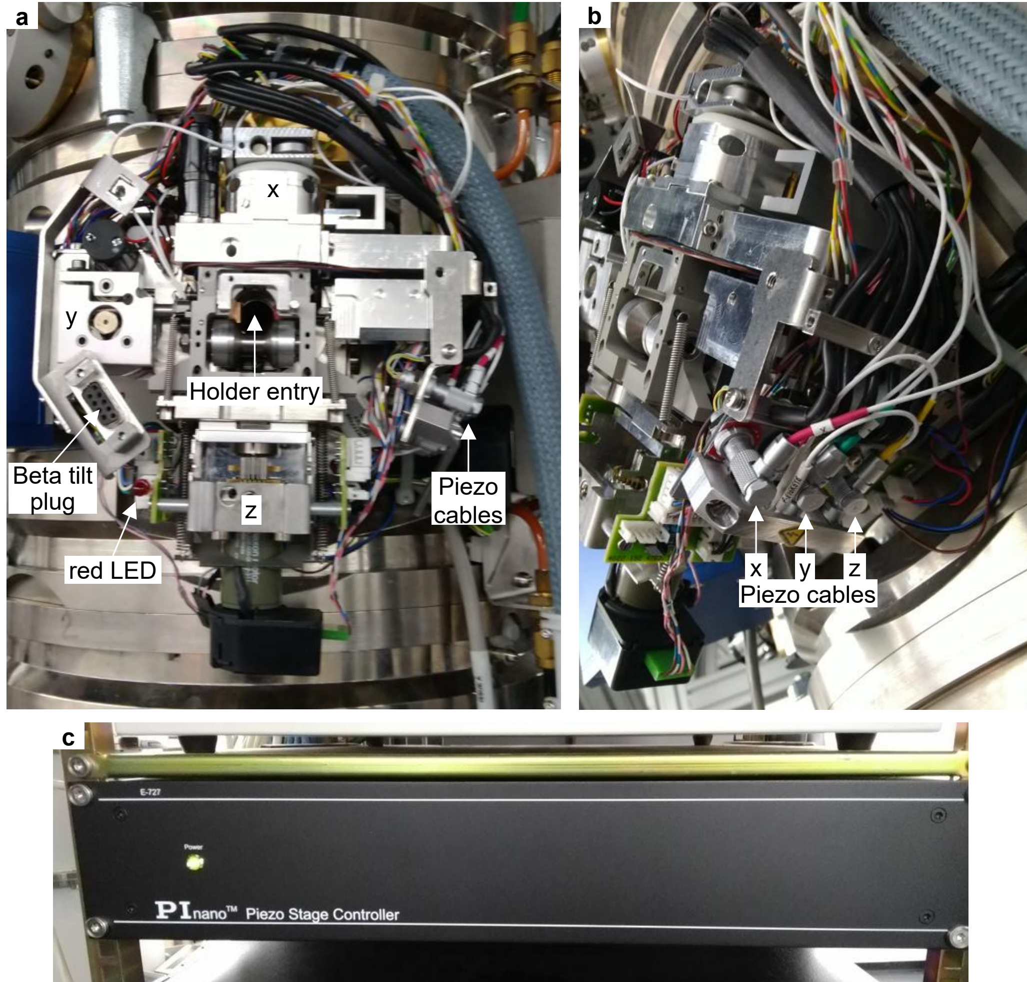

Figure S1: **Pictures of the piezo-enhanced compustage and its controller.** (a) Front-view picture of the compustage oriented at $\alpha = 0°$. (b) Side-view picture with the stage tilted at a large angle to show cables that control the x, y and z piezo components. (c) Electronic controller of the piezo stage.

Supplementary Information 3: Drift correction test using the mechanical and piezo stages

In order to compare the drift correction capabilities of the mechanical and piezo stages, tests have been performed using the two stages separately. Fig. S2(a) shows an image of a cross-grating replica sample with a field-of-view of approximately 600 nm and a pixel size of 0.16 nm. After a calibration step, a continuous correction of the position was set up using the mechanical stage only. Fig. S2(b) shows the distance with respect to the initial sample position and with pixel precision as a function of exposure time. Three displacements of approximately 50, 180 and 130 nm were introduced by moving the stage manually, as indicated by arrows in the plot. It can be observed that the mechanical stage is able to reduce the displacement below 10 nm (see magnified plot at the bottom). However, in the 10 nm range, the position of the sample does not change significantly. Displacements of up to 6 nm, as indicated by a dotted line, remain uncorrected, which suggests that the stage does not respond when such small movements are requested. Fig. S2(c) shows a similar plot obtained using the piezo stage. Again, three perturbations of approximately 50, 40 and 60 nm were introduced by moving the mechanical stage manually. Here, it can be observed that the piezo stage reacts in the sub-10 nm range and is able to reduce small displacements to zero after a few correction steps. The step-wise behavior is related to the fact that the correction factor was set to approximately 80% of the calibrated value. We found that this helps to converge more smoothly because the response of the stage is not always linear.

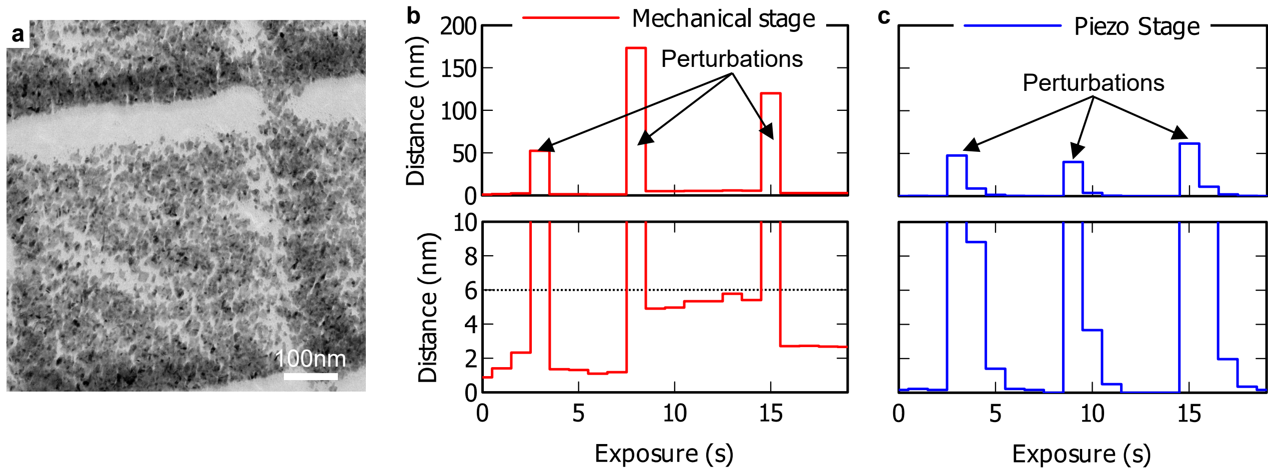

Figure S2: **Drift correction using the mechanical stage.** (a) TEM image of a cross-grating replica sample. (b) Plots that represent the displacement of the sample with respect to its initial position. Three perturbations were introduced as indicated by arrows. The correction is achieved using the mechanical stage. The bottom plot shows a magnified view of the bottom part of the profile. (c) Similar plot but using the piezo stage for correction.

73 # Supplementary Information 4: Calibration of the beam tilt

74 In order to calibrate the phase shift as a function of beam tilt, we have written a script that collects series of
75 holograms while incrementing the beam tilt with a predefined step. Fig. S3(a) is a schematic diagram that
76 illustrates the influence of the beam tilt on the position of the fringes. Fig. S3(b) is an example of electron
77 hologram obtained in the vacuum and Fig. S3(c) is the Fourier transform calculated in a small region of
78 the hologram, indicated by a dashed square, to minimize computation time. The coordinates of the pixel
79 that has the largest modulus in the side-band are then determined and the corresponding complex value
80 (composed of real Re and imaginary Im parts) is retrieved. For each beam tilt increment, the hologram and
81 the Fourier transform are updated and the phase $\phi = \arctan(Im/Re)$ associated to this pixel is plotted as
82 a function of the input value sent to the beam tilt θ coils (arbitrary units), as shown in Fig. S3(d). The
83 slope of the plot $\Delta\phi/\Delta\theta$ is then calculated to obtain the conversion factor between the phase and the beam
84 tilt. The calibration is performed twice in opposite tilt directions (positive and negative) and the average
85 slope is calculated. This can minimize errors in the case there is a drift of the biprism. In addition, since
86 there are two orthogonal pairs of beam tilt coils (x and y), their respective influence on the phase depends
87 on the orientation of the biprism in the xy plane. In this study, we have first tested the influence of the two
88 pairs of coils for a given orientation of the biprism and used the pair of coils that has the largest influence to
89 minimize the tilt.

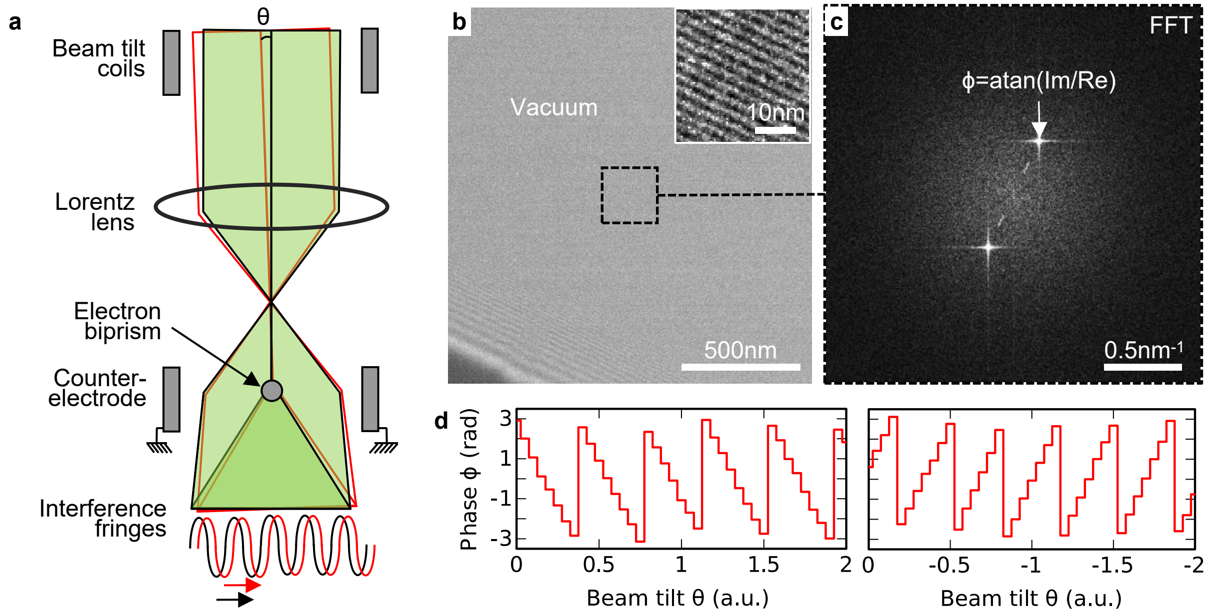

Figure S3: **Calibration of the beam tilt coils.** (a) Schematic diagram that illustrates the relation between the beam tilt θ and the position of the interference fringes in the hologram. (b) Example of electron hologram collected in the vacuum with an exposure time of 0.1 s. The inset in the top-right is a magnified image that shows interference fringes. (c) Fourier transform of the region indicated by a dashed square in (a) and displayed as the modulus of the complex terms. (d) Plots that show the phase (defined in radians and in a 2π range) associated to the pixel of the side-band that has the largest modulus, as a function of the input beam tilt θ (arbitrary unit) for positive and negative tilt directions and with a step of 0.05 a.u..

Supplementary Information 5: Calibration of the piezo stage

In order to calibrate the piezo stage, we have written a script that moves gradually the sample in a given direction and with a predefined increment. The position (x,y) of the sample in the hologram is then determined using cross-correlations of amplitude or phase images which are reconstructed automatically after the acquisition using Fourier transforms [6]. Fig. S4(a) is an example of hologram obtained on a cross-grating replica sample. To save computing time and to avoid possible perturbations from the edges of the holograms, only a small region of the hologram that contains distinct features is selected for the reconstruction. For instance, Fig. S4(b) is the amplitude image corresponding to the region indicated by a dashed square. Fig. S4(c) is a plot that shows the displacement of the sample in x and y directions in the image as a function of the input x_{piezo} value sent to the piezo stage (arbitrary units). For simplicity, it was assumed that the x and y axes are orthogonal and that the response is linear and identical for the two axis. A calibration factor c is determined from the slope of the modulus according to $c = \Delta\left(\sqrt{x^2+y^2}\right)/\Delta x_{\text{piezo}}$. The rotation angle α between the two coordinate systems is determined according to $\alpha = \arctan(y/x)$. Here the rotation angle is relatively small, approximately 0.2 rad, as shown in Fig. S4(d). The relationship between the coordinates of the piezo stage and the coordinates in the image is then obtained via a rotation matrix according to

$$\begin{aligned} x_{\text{piezo}} &= (x\cos(\alpha) + y\sin(\alpha))/c \\ y_{\text{piezo}} &= (-x\sin(\alpha) + y\cos(\alpha))/c\ . \end{aligned} \qquad (8)$$

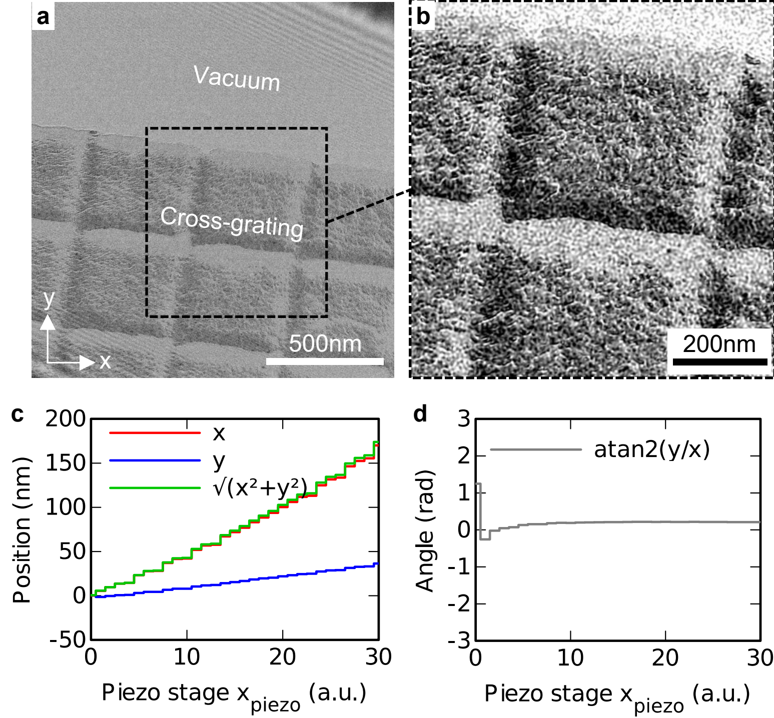

Figure S4: **Calibration of the piezostage.** (a) Example of electron hologram acquired on a cross-grating replica sample. (b) Amplitude image of the region indicated by a dashed square and reconstructed on-the-fly using Fourier transforms. (c) Plot that shows the displacement of the sample in (x,y) coordinates in the image as a function of the input x_{piezo} value of the piezo stage. The modulus $\sqrt{(x^2+y^2)}$ is also plotted. (d) Plot that shows the angle $\alpha = \arctan(y/x)$.

Supplementary Information 6: Acquisition of phase-shifted and double-resolution holograms

Series of phase-shifted holograms can be used to calculate phase images without Fourier transform and hence without aperture limiting the spatial resolution [7, 8]. After the calibration steps described in the previous section, the beam tilt coils were used to acquire phase-shifted holograms with a predefined phase shift and the piezo stage was used to maintain the sample at a fixed position during the acquisition. Fig. S5(a) shows an example of hologram of a cross-grating sample with a fringe spacing of 2.7 nm, a pixel size of 0.41 nm and an exposure time of 20 s. A phase-shifted series of four holograms was acquired with a shift of $\pi/2$ and Fig. S5(b) shows magnified images of the fringes in the vacuum region. For each phase shift, 100 holograms were collected with an individual exposure time of 0.2 s and summed directly during the acquisition. Fig. S5(c) shows three plots that represent the position of the fringes ϕ, the standard deviation of the phase $\delta\phi_{\mathrm{vac}}$ measured in the vacuum region (a corresponding phase image is shown in Fig. S5(d)) and the position of the sample (x,y) as a function of the exposure time. As expected, the phase profile shows four steps shifted by $\pi/2$ with a precision of ±0.1 rad. The profile of the standard deviation $\delta\phi_{\mathrm{vac}}$ shows that the noise decreases continuously with the exposure time and follows the same trend for the four shifts. The (x,y) position profile shows that the position of the sample remains stable with a precision of ±0.41 nm (pixel size), independently of the phase shift.

For a series of N holograms shifted by $2\pi/N$, the phase can be determined by the formula

$$\phi(x,y) = \arctan\left(\frac{\sum I_n \sin(2\pi n/N)}{\sum I_n \cos(2\pi n/N)}\right) - 2\pi q_{\mathrm{c}} x \ , \tag{9}$$

where I_n is the intensity distribution of the holograms, $n = 0, 1, ..., N-1$, q_{c} is the carrier frequency and x is the direction perpendicular to the biprism and to the optical axis [7]. Two phase images were then calculated using Fourier reconstruction of a single hologram and using direct calculation from the phase-shifted series. Fig. S5(e) shows a phase image of the cross-grating region indicated by a green dashed rectangle in (a), obtained using Fourier reconstruction with an aperture size of $q_{\mathrm{c}}/3$. Fig. S5(f) shows a phase image of the same region image obtained using Eq. 9. As expected, finer details can be observed in the last image compared to the previous one, which suggests a finer spatial resolution.

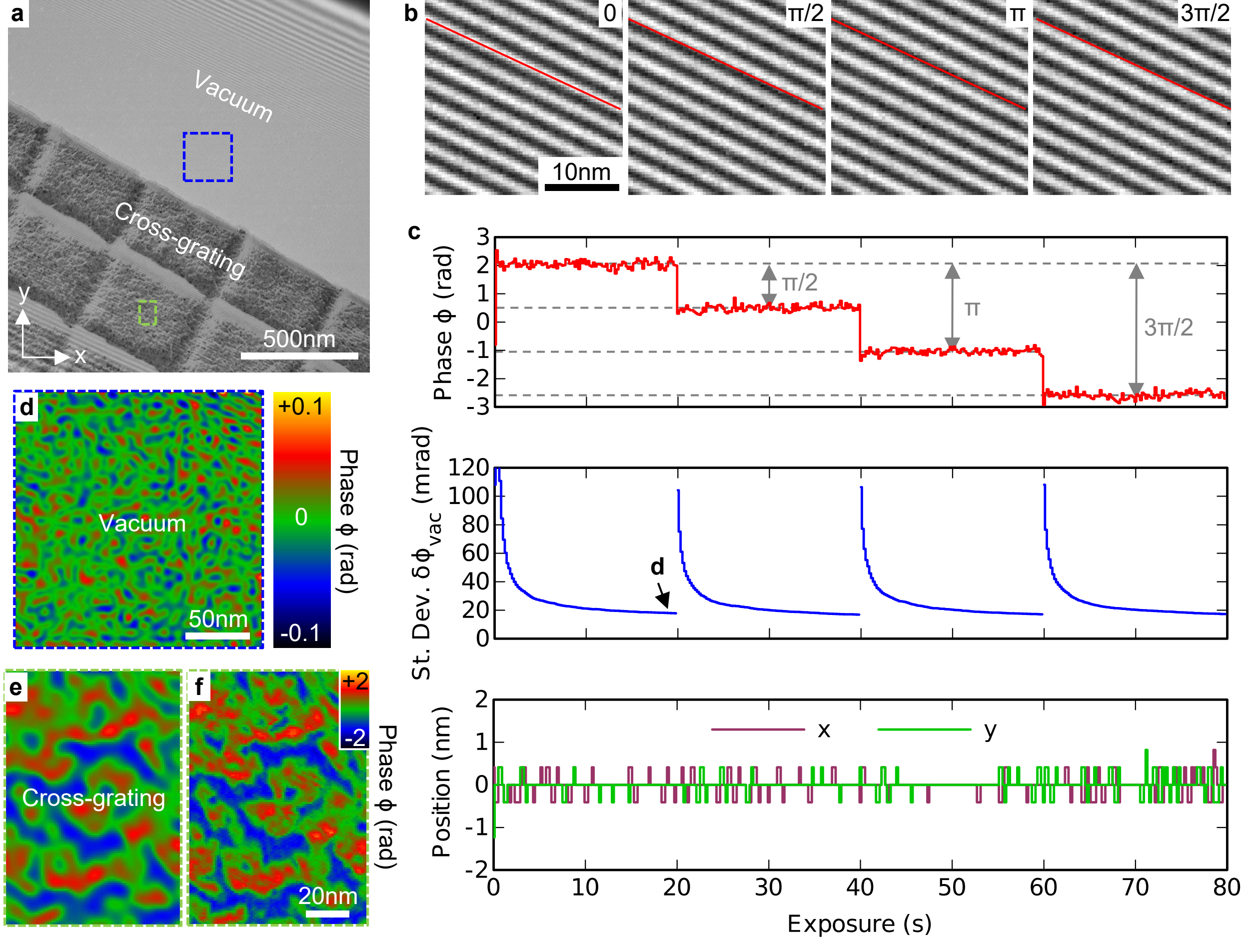

Figure S5: **Acquisition of a drift-corrected phase-shifted series.** (a) Example of electron hologram acquired on a cross-grating replica sample. (b) Magnified images of the interference fringes in four $\pi/2$-phase-shifted holograms. (c) Plots that show the position of the fringes ϕ, the standard deviation of the phase $\delta\phi_{\text{vac}}$ in the vacuum region and the position of the sample (x,y) as a function of exposure time. (d) Example of phase image calculated in the vacuum region indicated by a blue dashed square in (a) where $\delta\phi_{\text{vac}}$ was calculated. (e) Phase images of the cross-grating region indicated by a green dashed rectangle in (a) reconstructed from a single hologram using an aperture size of $q_c/3$. (f) Phase image of the same region reconstructed from the four phase-shifted holograms using direct calculation.

A special case of phase-shifted holography is called double-resolution where two π-shifted holograms are acquired and substracted [9]. This suppresses the center-band and hence allows the use of larger apertures in Fourier space as large as q_c instead of $q_c/3$ or $q_c/2$ for a standard hologram. However, the shift needs to be precisely π, otherwise the contrast of the fringes can be reduced. Fig. S6(a) shows a hologram of a cross-grating with a fringe spacing of 2.7 nm, a pixel size of 0.41 nm and an exposure time of 0.4 s. A magnified view of the fringes is shown on the right side. Fig. S6(b) is a double-resolution hologram obtained with 225 frames of 0.4 s (total exposure 90 s), which shows no background intensity but only variations of intensity caused by the fringes. This is related to the suppression of the center-band in the Fourier transform as shown in Fig. S6(c,d). Fig. S6(e) shows again three plots that represent the position of the fringes ϕ, the standard deviation of the phase $\delta\phi_{\text{vac}}$ measured in the vacuum region and the position of the sample (x,y) as a function of the exposure time. As shown by the phase profile ϕ, the fringes were shifted alternatively by

141 $+\pi/2$ and $-\pi/2$ between each individual frame of 0.4 s. The double-resolution hologram was then calculated
142 and displayed live during the acquisition. The standard deviation $\delta\phi_{\mathrm{vac}}$ decreases continuously and reaches
143 a similar value as previous ($\approx$ 10 mrad), which indicates there is no loss of contrast associated to the phase
144 shift. Again, the position of the sample (x,y) remained stable over the entire exposure thanks to the drift
145 correction provided by the piezo stage.

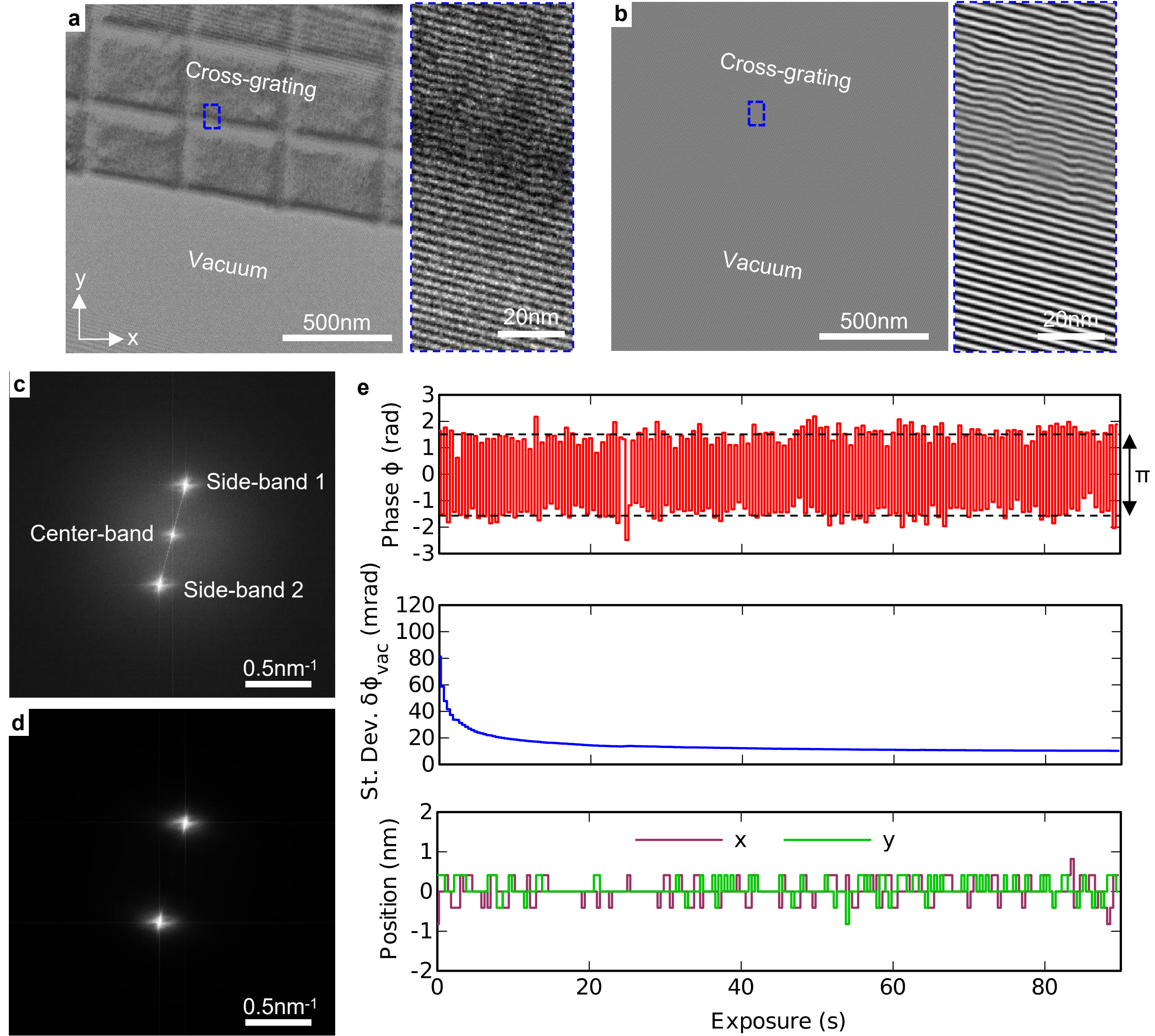

Figure S6: **Acquisition of a double-resolution hologram.** (a) Standard electron hologram acquired on a cross-grating replica sample with an exposure time of 0.4 s. A magnified view of the fringes in the dashed box is shown on the right side. (b) Double-resolution electron hologram of the same area obtained with 225 frames of 0.4 s (total exposure 90 s). (c,d) Fourier transforms of the hologram in (a,b). (e) Plots that show the position of the fringes ϕ, the standard deviation of the phase $\delta\phi_{\mathrm{vac}}$ in the vacuum region and the position of the sample (x,y) as a function of exposure time.

146 # Supplementary Information 7: Acquisition of holograms in objec-
147 tive mode

148 The experiments shown in the main article and in other sections of the supplement were carried out in
149 Lorentz mode with the excitation of the objective lens of the microscope set to zero. In order to test the
150 drift correction with finer fringes and hence finer spatial resolution, holograms were also acquired using the
151 standard TEM mode where the objective lens is excited. Fig. S7(a) shows an example of hologram obtained
152 on a cross-grating replica sample with a fringe spacing of 0.4 nm, a pixel size of 0.06 nm and a total exposure
153 time of 60 s, without drift correction. 300 frames with an individual exposure time of 0.2 s were collected and
154 summed during the acquisition. The sample is in the bottom-right part of the image and the top-left part
155 shows a vacuum region. Magnified images of the vacuum and sample regions (according to the rectangles in
156 (a)) are shown on the right side. Images with the same settings but with correction of the fringes and sample
157 position are shown in Fig. S7(c). Without correction, the holographic fringes are not visible in the vacuum
158 and only Fresnel fringes can be observed because the holographic fringe contrast is very weak $C = 0.3\%$.
159 With correction, the holographic fringes can be clearly observed with a contrast of $C = 13\%$. In both cases
160 crystal lattice fringes can be seen in the magnified image of the sample but the low mag image without
161 correction appears more blurry than the one with correction due to a drift of the sample. Fig. S7(b,d) shows
162 unwrapped phase images of the entire holograms in (a,c). Because of the very low fringe contrast in (a),
163 the uncorrected phase (b) shows a large number of unwrapping errors and a strong background noise with a
164 standard deviation of $\delta\phi_{\mathrm{vac}} = 928$ mrad in the vacuum region. On the other hand, the corrected phase (d)
165 is much smoother with $\delta\phi_{\mathrm{vac}} = 40$ mrad.

166 For more details, Fig. S7(e) show different plots that represent the position of the fringes ϕ, the standard
167 deviation of the phase $\delta\phi_{\mathrm{vac}}$ in the vacuum and the position of the sample (x,y) as a function of exposure
168 time. Without correction, the position of the fringes ϕ drifted several times over π, which causes the contrast
169 and hence the standard deviation $\delta\phi_{\mathrm{vac}}$ to oscillate. With correction, the position of the fringes ϕ remains
170 constant with a precision of ± 0.3 rad. $\delta\phi_{\mathrm{vac}}$ decreases continuously following an inverse relationship and tends
171 towards a limit of approximately 40 mrad. Regarding the position of the sample (x,y), without correction
172 the drift reached up to 2 nm in x and 12 nm in y during the entire experiment. With correction, the position
173 of the sample was maintained fixed with a precision of ± 0.2 nm.

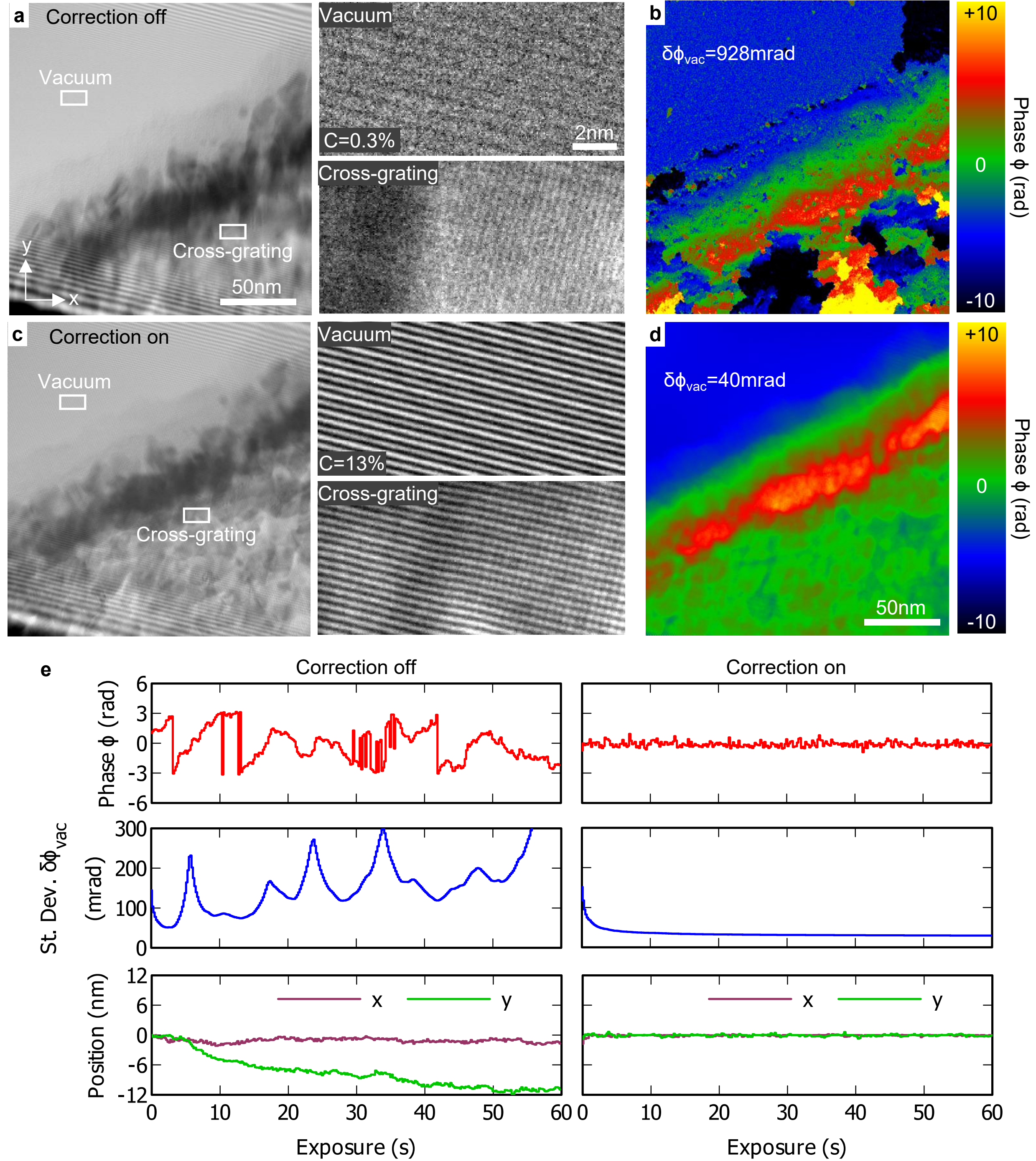

Figure S7: **Acquisition of holograms in objective mode.** (a) Off-axis electron hologram of a cross-grating replica sample recorded in objective mode for 60 s without any correction. Magnified images of the hologram in the vacuum and cross-grating region indicated by rectangles are shown on the right. (b) Corresponding phase image reconstructed using Fourier processing with an aperture size of $q_c/3$. (c) Off-axis electron hologram recorded for 60 s with correction of the fringe position using the beam tilt and correction of the sample position using the piezo stage. Magnified images of the hologram in the vacuum and cross-grating regions indicated by rectangles are shown on the right. (d) Corresponding phase image. (e) Plots that show the position of the fringes ϕ, the standard deviation of the phase $\delta\phi_{\mathrm{vac}}$ in the vacuum region and the position of the sample (x,y) as a function of exposure time, without (left) and with correction (right).

174 # Supplementary Information 8: Cross-correlation of images reconstructed from holograms of a transistor

176 In order to find correct settings for the cross-correlation of images of transistors shown in the main article
177 (in section 3.3.2) , preliminary tests have been performed with different images. Fig. S8(a) shows a hologram
178 of a transistor and reconstructed images including the intensity $I_{\mathrm{rec}}(\vec{r})$, the amplitude $A_{\mathrm{rec}}(\vec{r})$ and the phase
179 $\phi_{\mathrm{rec}}(\vec{r})$ as described in Eq. 3. In Fig. S8(b), the hologram was shifted numerically by approximately 170 nm,
180 as indicated by a white arrow. The same series of images was reconstructed from the shifted hologram.
181 Cross-correlations were then performed for each type of image as shown in Fig. S8(c). The arrows indicate
182 the position of the maximum. It was found that only the cross-correlation of the phase images (ϕ_{rec}) shown
183 in the last column gives the correct value of the shift. The other images led to distant results.

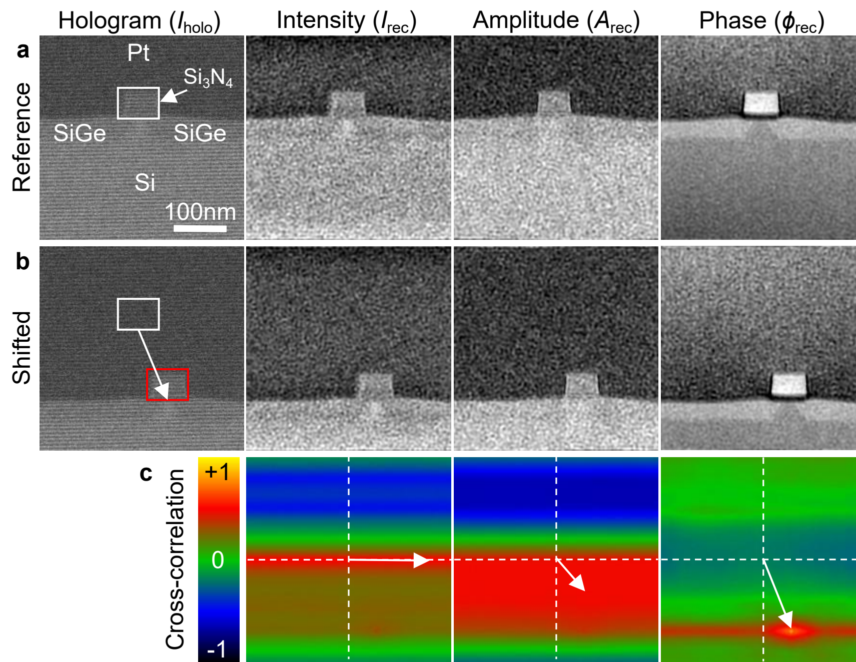

Figure S8: **Cross-correlation of images of transistors.** (a) Off-axis electron hologram of a dummy MOSFET transistor and reconstructed images including the intensity $I_{\mathrm{rec}}(\vec{r})$, the amplitude $A_{\mathrm{rec}}(\vec{r})$ and the phase $\phi_{\mathrm{rec}}(\vec{r})$. (b) Same hologram as in (a) but shifted by 170 nm, as indicated by a white arrow, and corresponding series of reconstructed images. (c) Corresponding series of cross-correlation images where the arrows indicate the position of the maximum.

184 # References

185 [1] H. Lichte, M. Lehmann, Electron holography - basics and applications, Reports on Progress in Physics
186 71 (1) (2008) 016102. doi:10.1088/0034-4885/71/1/016102.
187 URL https://doi.org/10.1088/0034-4885/71/1/016102

188 [2] M. R. McCartney, D. J. Smith, Electron holography: Phase imaging with nanometer resolution, Annual
189 Review of Materials Research 37 (1) (2007) 729–767. doi:10.1146/annurev.matsci.37.052506.084219.
190 URL https://doi.org/10.1146/annurev.matsci.37.052506.084219

191 [3] D. Lei, K. Mitsuishi, K. Harada, M. Shimojo, D. Ju, M. Takeguchi, Direct acquisition of interferogram by
192 stage scanning in electron interferometry, Microscopy 62 (6) (2013) 563–570. doi:10.1093/jmicro/dft032.
193 URL https://doi.org/10.1093/jmicro/dft032

194 [4] D. Lei, K. Mitsuishi, K. Harada, M. Shimojo, D. Ju, M. Takeguchi, Super-resolution phase reconstruction
195 technique in electron holography with a stage-scanning system, Japanese Journal of Applied Physics
196 53 (2S) (2014) 02BC23. doi:10.7567/jjap.53.02bc23.
197 URL https://doi.org/10.7567/jjap.53.02bc23

198 [5] M. Takeguchi, A. Hashimoto, M. Shimojo, K. Mitsuishi, K. Furuya, Development of a stage-scanning
199 system for high-resolution confocal STEM, Journal of Electron Microscopy 57 (4) (2008) 123–127.
200 doi:10.1093/jmicro/dfn010.
201 URL https://doi.org/10.1093/jmicro/dfn010

202 [6] E. Völkl, L. F. Allard, B. Frost, A software package for the processing and reconstruction of electron
203 holograms, Journal of Microscopy 180 (1) (1995) 39–50. doi:10.1111/j.1365-2818.1995.tb03655.x.
204 URL https://doi.org/10.1111/j.1365-2818.1995.tb03655.x

205 [7] Q. Ru, J. Endo, T. Tanji, A. Tonomura, Phase-shifting electron holography by beam tilting, Applied
206 Physics Letters 59 (19) (1991) 2372–2374. doi:10.1063/1.106019.
207 URL https://doi.org/10.1063/1.106019

208 [8] Q. Ru, G. Lai, K. Aoyama, J. Endo, A. Tonomura, Principle and application of phase-shifting electron
209 holography, Ultramicroscopy 55 (2) (1994) 209–220. doi:10.1016/0304-3991(94)90171-6.
210 URL https://doi.org/10.1016/0304-3991(94)90171-6

211 [9] V. Volkov, M. Han, Y. Zhu, Double-resolution electron holography with simple Fourier transform of
212 fringe-shifted holograms, Ultramicroscopy 134 (2013) 175–184. doi:10.1016/j.ultramic.2013.06.018.
213 URL https://doi.org/10.1016/j.ultramic.2013.06.018